

See discussions, stats, and author profiles for this publication at: <https://www.researchgate.net/publication/326822322>

High Mobility Indium Oxide Electron Transport Layer for Efficient Charge Extraction and Optimized Nano-Morphology in Organic Photovoltaics

Article in *Nano Letters* · August 2018

DOI: 10.1021/acs.nanolett.8b02452

CITATIONS

34

READS

442

13 authors, including:



Wenchao Huang

Wuhan University of Technology

88 PUBLICATIONS 7,912 CITATIONS

SEE PROFILE



Bowen Zhu

Westlake University

105 PUBLICATIONS 8,686 CITATIONS

SEE PROFILE



Sheng-Yung Chang

University of California, Los Angeles

25 PUBLICATIONS 3,309 CITATIONS

SEE PROFILE



Pei Cheng

Sichuan University

116 PUBLICATIONS 9,036 CITATIONS

SEE PROFILE

High Mobility Indium Oxide Electron Transport Layer for an Efficient Charge Extraction and Optimized Nanomorphology in Organic Photovoltaics

Wenchao Huang,^{†,‡} Bowen Zhu,^{†,‡} Sheng-Yung Chang,^{†,‡} Shuanglin Zhu,^{†,‡} Pei Cheng,^{†,‡} Yao-Tsung Hsieh,^{†,‡} Lei Meng,^{†,‡} Rui Wang,^{†,‡} Chaochen Wang,^{†,‡} Chenhui Zhu,[§] Christopher McNeill,^{||} Mingkui Wang,[⊥] and Yang Yang^{*,†,‡,||}

[†]Department of Materials Science and Engineering, University of California, Los Angeles, California 90095, United States

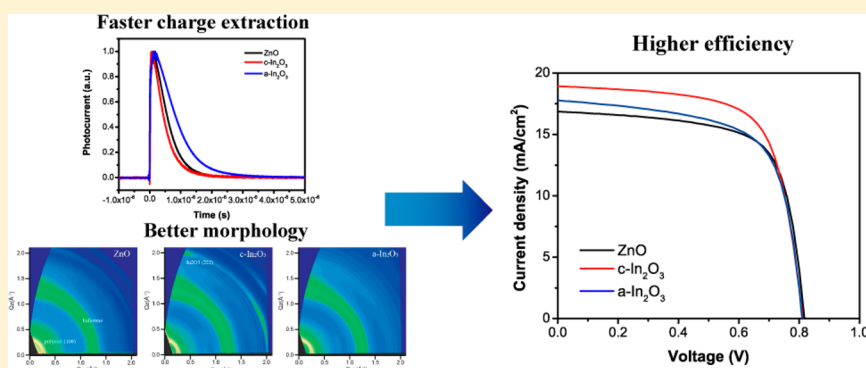
[‡]California NanoSystems Institute, University of California, Los Angeles, California 90095, United States

[§]Advanced Light Source, Lawrence Berkeley National Laboratory, Berkeley, California 94720, United States

^{||}Department of Materials Science and Engineering, Monash University, Clayton, Victoria 3800, Australia

[⊥]Wuhan National Laboratory for Optoelectronics, Huazhong University of Science and Technology, Wuhan 430070, People's Republic of China

Supporting Information



ABSTRACT: The electron transport layer (ETL) plays an important role in determining the device efficiency of organic solar cells (OSCs). A rational design of an ETL for OSCs targets high charge extraction and induction of an optimized active layer morphology. In this Letter, a high mobility In_2O_3 synthesized via a solution-processed combustion reaction is successfully used as a universal ETL in an organic photovoltaic device. With the modification of a thin layer of polyethylenimine ethoxylated (PEIE), a device based on crystalline In_2O_3 outperforms its counterpart, ZnO, in both PBDTTT-EFT-based fullerene and nonfullerene systems. As ZnO is replaced by In_2O_3 , the average efficiency increases from 9.5% to 10.5% for PBDTTT-EFT- PC_{71}BM fullerene-based organic solar cells and also increases from 10.8% to 11.5% for PBDTTT-EFT-IEICO-4F nonfullerene-based organic solar cells, respectively. Morphological studies have unraveled the fact that the crystalline In_2O_3 ETL with highly aligned nanocrystallites has induced the crystallization of polymer into a preferential molecular packing that favors the charge transport across an active layer. From the photophysical study, it is found that charge extraction in the crystalline In_2O_3 device is significantly faster than in the ZnO device due to the higher mobility of In_2O_3 and optimized nanomorphology of the active layer.

KEYWORDS: Organic solar cells, electron transport layer, indium oxide, morphology, charge extraction

Converting solar energy into electrical energy is a promising technique that would satisfy the rapidly increasing demand for clean energy.^{1–7} Among various photovoltaic technologies, organic solar cells (OSCs) have attracted an increasing interest in both academia and industry in the last few decades. OSCs offer advantages of a low-cost solution processing and potential of manufacturing flexible substrates. With the development of novel materials and

optimization of active layer morphology, device efficiency of OSCs has already surpassed 14% recently.^{8–13}

Most of OSCs are based on a bulk-heterojunction (BHJ) structure, where electron-donor and -acceptor materials are mixed within the active layer.¹⁴ This architecture consists of

Received: June 17, 2018

Revised: July 24, 2018

Published: August 3, 2018

interpenetrating networks of electron-donor and electron-acceptor materials, providing a large interfacial area where efficient exciton separation can occur. This BHJ active layer is typically sandwiched between an electron transport layer (ETL) and a hole-transport layer (HTL) to minimize charge recombination at both interfaces and facilitate charge extraction. Hence, the selection of proper interfacial layers is critical for the high performance of OSCs.

Inverted device architecture is widely used in highly efficient OSCs because of its better stability and optimized vertical phase separation.^{15–17} In the inverted structure, the ETL plays an important role in determination of device performance. The ETL can not only enhance electron extraction and reduce charge recombination but also influence the morphology of active layer. The metal oxide-based ETLs specifically have attracted immense attention due to their highly transparent nature and tunable energy levels and electrical properties achieved through doping or chemical modification.¹⁸ A number of metal oxides such as pristine and doped ZnO^{19–22} and TiO₂^{21,23} have been already synthesized and employed in the inverted OSCs. However, both ZnO- and TiO₂-based ETLs suffer from their relative low mobility. Hence, it is necessary to develop a high mobility alternative metal oxide such as SnO₂ and In₂O₃ for facilitating charge extraction and achieving a better device efficiency.^{24,25}

In this Letter, we report a solution-processed high mobility In₂O₃ ETL. The In₂O₃ ETL is achieved by using indium nitrate hydrate as a precursor mixed with a small amount of additives to lower its annealing temperature below 300 °C via a combustion reaction.^{26,27} By rational selection of metal oxide precursors and additives, a strong exothermic combustion reaction can be stimulated to form high quality In₂O₃ films at low temperatures, facilitating the subsequent fabrication processes of OSCs.²⁸ The two design rules for an excellent ETL are to be able to collect the electron charge carrier in an efficient way and to induce a favorable active layer morphology. The solution-processed In₂O₃ incorporates both of these two aspects. The mobility of In₂O₃ increases up to 15 cm²/(V·s), which is 1 order of magnitude higher than the one of solution-processed ZnO, which can significantly improve the charge extraction. In addition, by combining the microscopy and scattering results, it becomes clear that the crystalline In₂O₃ layer exhibits a preferential orientation with the (222) plane either parallel or perpendicular to the glass substrate, which consequently induces crystallization of the polymer into a highly ordered crystallite orientation.

A model system, the blend of poly[[2,60–4,8-di(5-ethylhexylthienyl)benzo[1,2-*b*;3,3-*b'*]dithiophene]3-fluoro-2[(2-ethylhexyl)carbonyl]thieno[3,4-*b'*]thiophenediyl] (PBDTTT-EFT, also called PTB7-Th) with PC₇₁BM (shown in Figure 1a), is used to compare the device performance based on three different ETLs: crystalline In₂O₃ (c-In₂O₃, annealed at 300 °C), amorphous In₂O₃ (a-In₂O₃, annealed at 200 °C), and ZnO (annealed at 200 °C).^{29–32} As shown in Figure 1b, devices are fabricated with a structure of ITO/ETL/PEIE/PBDTTT-EFT–PC₇₁BM/MoO₃/Ag. A thin layer of PEIE is used to tune the work function of metal oxide for a better charge extraction and minimize the pinhole density in the In₂O₃ ETL.³³ Devices based on the PEIE-modified c-In₂O₃ exhibit an average power conversion efficiency (PCE) of 10.5%, showing an enhancement by over 10% compared with its PEIE-modified ZnO counterpart. The photocurrent decay measurement reveals an improved charge extraction in the c-

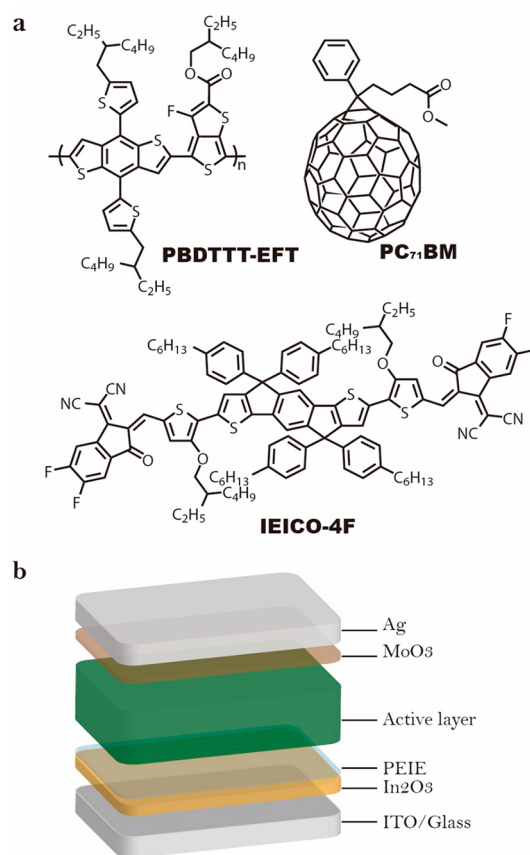


Figure 1. (a) Molecular structure of PBDTTT-EFT (also called PTB7-Th), PC₇₁BM, and IEICO-4F. (b) Schematic of the inverted organic solar cell based on a structure of ITO/In₂O₃/PEIE/active layer/MoO₃/Ag.

In₂O₃ device. In addition to PBDTTT-EFT–PC₇₁BM fullerene-based solar cells, devices based on c-In₂O₃ also show the superior photovoltaic performance compared to the devices based on ZnO in PBDTTT-EFT–IEICO-4F nonfullerene solar cells. An average efficiency of 11.5% is achieved by using the c-In₂O₃ ETL in PBDTTT-EFT–IEICO-4F solar cells.

Results and Discussion. ETLs need to be highly transparent for sufficient light transmittance. In₂O₃ is, thus, a suitable candidate because it exhibits a large energy gap greater than 3 eV.³⁴ The transmission spectrum (Figure 2a) shows that c-In₂O₃ film has a very low absorption in the visible region. The transmittance in the region between 400 and 800 nm is above 95%. The c-In₂O₃ crystals are homogeneous and compactly packed on the surface of ITO (Figure 2b). From lab-based X-ray diffraction results (Figure 2c), the occurrence of crystallization is observed in In₂O₃ film annealed at 300 °C. The peak located at $2\theta = 30.6^\circ$ corresponds to the scattering from the (222) peak. However, due to the too thin of c-In₂O₃ film and low X-ray flux, a low scattering intensity is observed in the lab-based X-ray scattering measurement. A synchrotron-based grazing incidence wide-angle X-ray scattering (GI-WAXS) is also employed to further probe the crystallization behavior of the c-In₂O₃ film with a significantly higher X-ray flux. The crystallite information, such as the crystallite orientation, could also be monitored using a 2D detector. From the 2D scattering pattern of c-In₂O₃ film (Figure 2d), a strong intense peak at $q = 2.1 \text{ \AA}^{-1}$ corresponds to the (222) plane. This (222) scattering peak can be observed only along

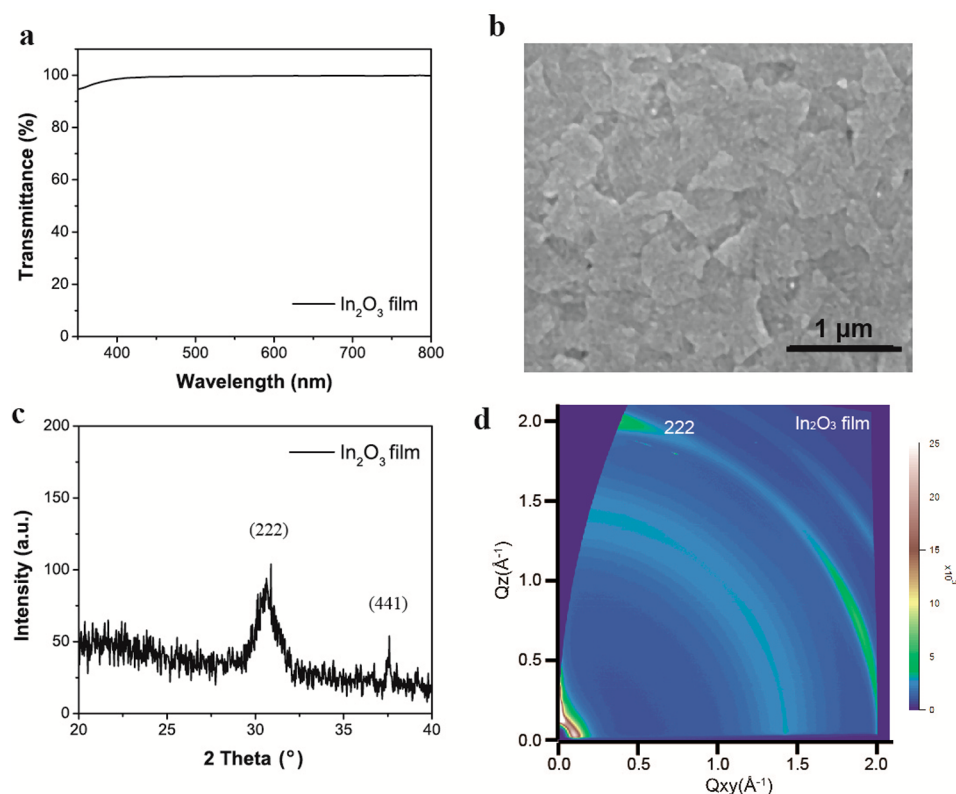


Figure 2. Optical properties and morphology of In_2O_3 thin film. (a) Transmittance spectra of c- In_2O_3 film on the glass substrate. (b) Scanning electron microscope (SEM) image of c- In_2O_3 film on the ITO coated glass. (c) Lab-based X-ray diffraction (XRD) spectra of the c- In_2O_3 film. (d) Grazing incidence wide-angle X-ray scattering (GIWAXS) pattern of the c- In_2O_3 film.

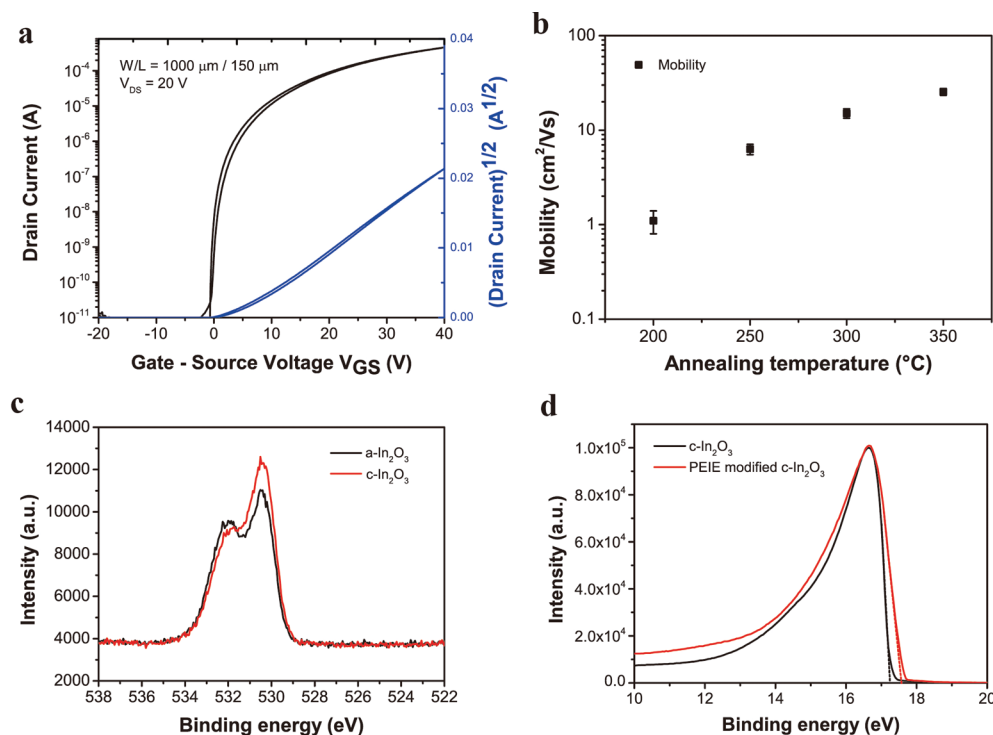


Figure 3. Electrical properties of In_2O_3 thin film. (a) Electrical performance of c- In_2O_3 thin-film transistors (TFT). The device structure is bottom-gate and top-contact, and the c- In_2O_3 thin film is annealed at 300 $^\circ\text{C}$. (b) The saturation mobility of In_2O_3 TFT as a function of annealing temperature. (c) X-ray photoelectron spectroscopy (XPS) O 1s spectra of c- In_2O_3 and a- In_2O_3 . (d) Ultraviolet photoelectron spectroscopy (UPS) spectra of c- In_2O_3 modified with and without PEIE.

the out-of-plane (OOP) or in-plane (IP) direction, suggesting that the (222) plane of In_2O_3 crystallites is either parallel or perpendicular to the substrate. As the annealing temperature decreases to 200 °C, the In_2O_3 film shows a totally amorphous microstructure. There is no scattering peak from the a- In_2O_3 film annealed at 200 °C in both lab-based and synchrotron-based scattering measurements; see Figures S1 and S2.

In order to characterize the electrical performance of In_2O_3 films, In_2O_3 -based thin-film transistors (TFTs) were fabricated with a bottom-gate and top-contact (BGTC) structure. A typical transfer curve of c- In_2O_3 TFT is illustrated in Figure 3a, with an annealing temperature at 300 °C. Extracted from this transfer curve, the mobility of In_2O_3 film annealed at 300 °C is measured to be 15.1 $\text{cm}^2/(\text{V}\cdot\text{s})$. The device shows a turn-on voltage at around 0 V and a high on/off ratio of 10^7 . The mobility increases to 25.5 $\text{cm}^2/(\text{V}\cdot\text{s})$ as the annealing temperature is increased to 350 °C, as illustrated in Figure 3b. The amorphous In_2O_3 TFTs annealed at 200 °C also show a high saturation mobility of about 1.0 $\text{cm}^2/(\text{V}\cdot\text{s})$.

The oxygen binding state plays an important role in determining the mobility of the In_2O_3 films.³⁴ Figure 3c compares the X-ray photoelectron spectroscopy (XPS) O 1s spectrum of c- In_2O_3 and a- In_2O_3 films. There are two peaks located at 532.1 and 530.4 eV, representing the hydroxide bonding and oxide lattice, respectively.²⁸ Compared with the a- In_2O_3 film, the peak area related to the oxide lattice shows a dramatic increase in the c- In_2O_3 film, confirming a better crystalline microstructure. Meanwhile, the peak area corresponding to the hydroxide bonding slightly decreases in the c- In_2O_3 film. In this study, in order to further improve the charge extraction at the interface between the ETL and active layer, all ETLs are modified by using a dipole layer PEIE, which allows for tuning of their work functions and reducing pinhole defects.^{33,35} The work functions of c- In_2O_3 film modified with and without PEIE are measured by ultraviolet photoemission spectroscopy (UPS), as shown in Figure 3d. The UPS spectra reveal that the work function of c- In_2O_3 film decreases 0.4 V after modification of the thin layer of PEIE, improving the charge injection at the interface between the ETL and active layer.

All devices were fabricated with an inverted structure of ETL/PEIE/active layer/ MoO_3/Ag . The active layers were prepared by using the same solution with a donor/acceptor weight ratio of 1:1.5. Figure 4 presents the average photovoltaic performance of organic solar cells based on different ETLs: ZnO, c- In_2O_3 , and a- In_2O_3 . (All of the photovoltaic parameters are summarized in Table 1.) Figure 4a plots the current–voltage (J - V) characteristics under a light intensity of 100 mW/cm^2 . The devices based on ZnO exhibit an average PCE of 9.5% with a short circuit current (J_{sc}) of 16.9 mA/cm^2 , an open-circuit voltage (V_{oc}) of 0.82 V and a fill factor (FF) of 0.69. When ZnO is replaced by c- In_2O_3 (annealed at 300 °C), the device PCE shows an enhancement by over 10%, significantly increasing from 9.5% to 10.5%. The main reason for the improved device performance is attributed to the increased J_{sc} from 16.9 to 18.9 mA/cm^2 . From the external quantum efficiency (EQE) measurement (Figure 4b), it is noted that the EQE spectra of the device based on c- In_2O_3 show higher values over the whole visible region between 400 and 800 nm. The maximum EQE value in the c- In_2O_3 device reaches over 80% at the wavelength of 725 nm. The integrated J_{sc} values from EQE spectra are 16.4 mA/cm^2 for ZnO and 18.4 mA/cm^2 for c- In_2O_3 , respectively. (The difference

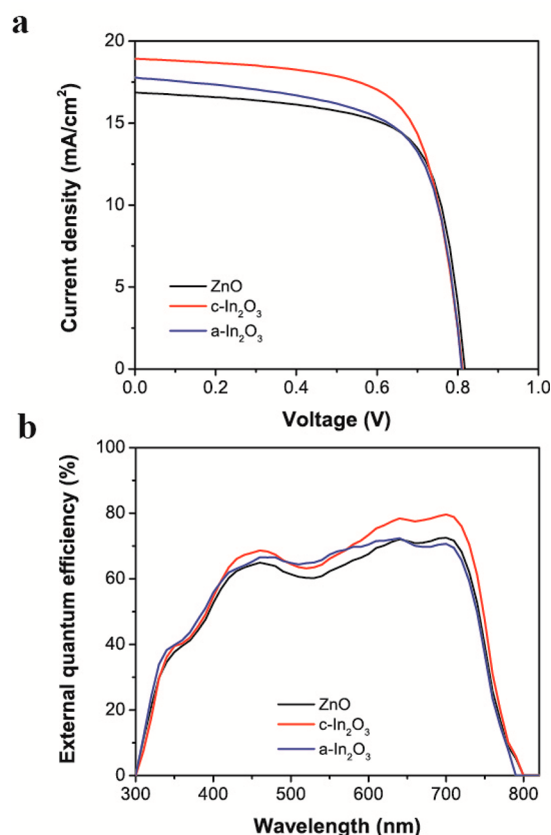


Figure 4. Device performance of PBDTTT-EFT- PC_{71}BM organic solar cells based on various ETLs: ZnO, c- In_2O_3 , and a- In_2O_3 . (a) Current density–voltage (J - V) curve and (b) external quantum efficiency (EQE) spectra.

between J_{sc} values measured from J - V curves and integrated from EQE spectra is less than 5%.) The enhancement in the integrated EQE value shows a good agreement with the enhancement in J_{sc} .

The PCEs of devices based on the In_2O_3 ETL are sensitive to the annealing temperature. As the annealing temperature is decreased to 200 °C, the efficiency slightly decreased to 9.5%, which is similar to the one in devices based on the ZnO ETL. The device yields a J_{sc} of 17.7 mA/cm^2 (17.1 mA/cm^2 calculated from EQE), a V_{oc} of 0.81 V, and a fill factor of 0.66. As shown in Figure S4, device PCEs show a monotonical increase with the annealing temperature in the region between 200 and 300 °C. The change in device performance is mainly attributed to the mobility of the In_2O_3 ETL. As the annealing temperature continues to increase to 350 °C, the mobility of In_2O_3 further increases to 25 $\text{cm}^2/(\text{V}\cdot\text{s})$, while the PCE slightly decreases to 10.2%. The possible explanations to this phenomenon are the formation of plenty of pinholes in In_2O_3 films and the increase of ITO resistance under such high temperature annealing.

In addition to the PBDTTT-EFT- PC_{71}BM fullerene-based system, we also compare device performance of a nonfullerene system based on different ETLs (see Figure S5). The device fabricated on ZnO shows an average efficiency of 10.8% with a J_{sc} of 22.1 mA/cm^2 , a V_{oc} of 0.71 V, and a fill factor of 0.69. The device based on a- In_2O_3 shows a similar average efficiency compared to the one based on ZnO. Among three different ETLs, the highest average efficiency (11.5%) is achieved in a device based on c- In_2O_3 . Similar to the PBDTTT-EFT-

Table 1. Average Device Performance of Organic Solar Cells Based on Various ETLs

active layer	ETL	efficiency (%)	V_{OC} (V)	J_{sc} (mA/cm ²)	fill factor	R_s (Ω cm ²)	R_{sh} (Ω cm ²)
PBDTTT-EFT-PC ₇₁ BM	ZnO	9.5 (± 0.2)	0.82 (± 0.1)	16.9 (± 0.2)	0.69 (± 0.2)	5.0	803
PBDTTT-EFT-PC ₇₁ BM	c-In ₂ O ₃	10.5 (± 0.3)	0.81 (± 0.2)	18.9 (± 0.5)	0.69 (± 0.3)	4.7	821
PBDTTT-EFT-PC ₇₁ BM	a-In ₂ O ₃	9.5 (± 0.4)	0.81 (± 0.1)	17.7 (± 0.4)	0.66 (± 0.3)	4.6	624
PBDTTT-EFT-IEICO-4F	ZnO	10.8 (± 0.3)	0.71 (± 0.1)	22.1 (± 0.3)	0.69 (± 0.2)	3.2	456
PBDTTT-EFT-IEICO-4F	c-In ₂ O ₃	11.5 (± 0.3)	0.71 (± 0.2)	23.7 (± 0.4)	0.68 (± 0.3)	2.8	414
PBDTTT-EFT-IEICO-4F	a-In ₂ O ₃	10.8 (± 0.4)	0.71 (± 0.1)	22.3 (± 0.4)	0.68 (± 0.2)	2.9	402

PC₇₁BM blend, the c-In₂O₃ device also exhibits the highest J_{sc} among PBDTTT-EFT-IEICO-4F solar cells. Compared with the ZnO device, the J_{sc} of the c-In₂O₃ device increases to 23.7 mA/cm². The increased short circuit current is also the main reason for the efficiency improvement in this nonfullerene solar cell.

In order to probe the effect of the underlying layer on the active layer nanomorphology and device physics, the PBDTTT-EFT-PC₇₁BM blend was taken as a model system to investigate the crystallization behavior of the polymer (i.e., crystalline orientation) and charge extraction at the interface between the ETL and active layer.^{36,37} The two-dimensional GIWAXS scattering patterns of PBDTTT-EFT-PC₇₁BM blends based on three different ETLs (ZnO, c-In₂O₃, and a-In₂O₃) are presented in Figure 5a–c. A prominent (100) reflection is found at $q = 0.31 \text{ \AA}^{-1}$, which corresponds to alkyl stacking.^{32,35} From the peak position, the alkyl stacking distance is calculated to be 2.03 Å, which is similar to our previous measurement.^{35,38} The (100) reflection in both In₂O₃ samples shows the significantly higher intensity than the ZnO sample. The coherence length of polymer crystallite is calculated from full width at half maximum (fwhm) of scattering peak by using the Scherrer equation. The fitted parameter of polymer (100) peak is summarized in Table S1. Polymer deposited on both In₂O₃ ETLs shows a large coherence length (8.2 nm for c-In₂O₃ and 8.1 nm for a-In₂O₃) than that on ZnO (7.6 nm). This suggests that the In₂O₃-based ETLs can facilitate the crystallization of polymer PBDTTT-EFT.

In addition to crystallinity, the orientation of polymer crystallites is also important for the charge transport. The pole figure of polymer (100) peak is extracted from 2D scattering patterns, as shown in Figure S6. The polymer films on ZnO and a-In₂O₃ show a similar crystallite orientation that polymer crystallites are almost randomly oriented with a slightly higher intensity along the in-plane direction. However, from the scattering pattern of the c-In₂O₃ sample, it is worth noting that the significantly higher intensities are found along either the out-of-plane or in-plane direction, indicating that the polymer PBDTTT-EFT on the c-In₂O₃ substrate exhibits more aligned crystallites. Such observation could be explained by the substrate-induced polymer crystallization. The scattering peak located at $q = 2.1 \text{ \AA}^{-1}$ is identified as the (222) peak from the c-In₂O₃ film. The (222) c-In₂O₃ peak is largely located along either out-of-plane or in-plane axis, indicating that the oriented crystallites are observed in the c-In₂O₃ film. The highly aligned c-In₂O₃ crystallites have led to the crystallization of polymer PBDTTT-EFT with more ordered orientations. ZnO and In₂O₃ ETLs are modified with a layer of PEIE to tune their work function and minimize pinhole density. The existence of this ultrathin layer could partially compensate the benefit of the underlying In₂O₃ layer on the polymer morphology. However, the thickness of this PEIE layer is less than 10 nm.

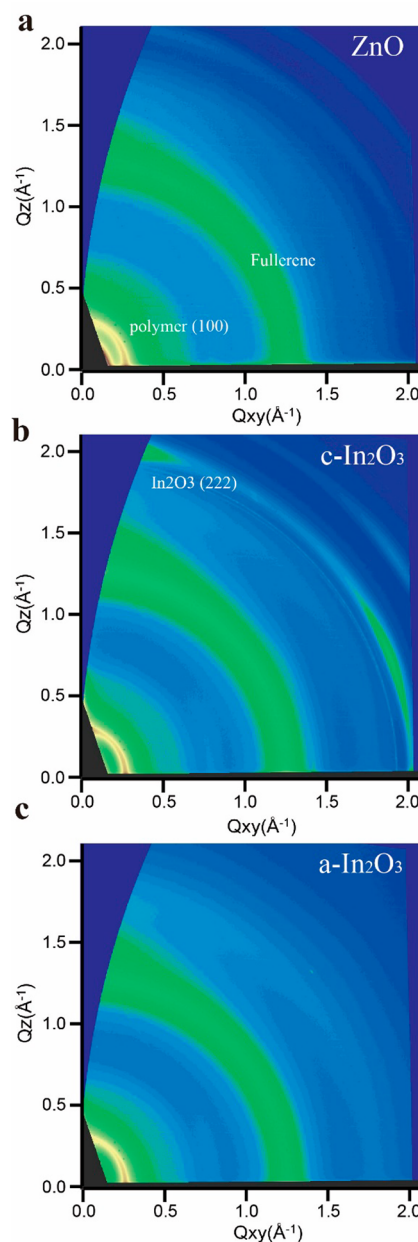


Figure 5. 2D GIWAXS scattering patterns of PBDTTT-EFT-PC₇₁BM blend on different ETLs: (a) ZnO, (b) c-In₂O₃, and (c) a-In₂O₃.

The crystallization behavior of polymer PBDTTT-EFT is still strongly dependent on the microstructure of the underlying metal oxide.

A broad out-of-plane peak located at $q = 1.5 \text{ \AA}^{-1}$ corresponding to the polymer π - π stacking can be also observed from 2D scattering patterns, but the peak position of

the scattering pattern from polymer π - π stacking is close to that from fullerene molecules. In order to distinguish these two peaks, line profiles (out-of-plane and in-plane) are extracted from the 2D scattering patterns by integrating the scattering intensity along the out-of-plane and in-plane directions. (The integration area is shown in Figure S7.) As shown in the 1D out-of-plane scattering profiles (Figure S8), the peak intensity of polymer π - π stacking located at $q = 1.5 \text{ \AA}^{-1}$ in the c-In₂O₃ sample is stronger than that in the a-In₂O₃ and ZnO samples. It indicates that the highly oriented c-In₂O₃ underlying layer leads to the polymer crystallization into a more “face-on” configuration with the π - π stacking direction perpendicular to the substrate. As the charge transport through the π - π stacking direction is faster than that through the side-chain direction, the face-on configuration is considered as a favorable morphology for the efficient charge transport. Combination of the highly ordered crystallite orientation and increased face-on configuration facilitates the charge transport and minimizes the charge recombination possibility in the c-In₂O₃ device.

The charge extraction with different ETLs is investigated with a transient photocurrent measurement (TPC), shown in Figure 6. In this measurement, a constant background

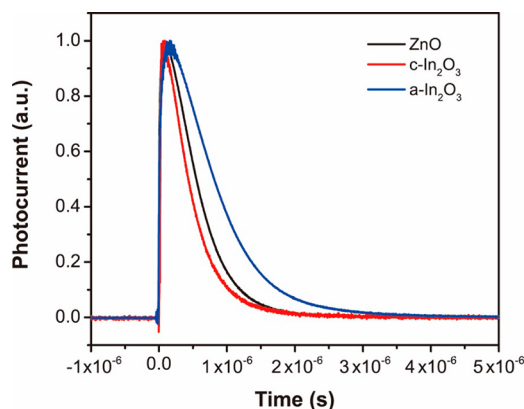


Figure 6. Photocurrent decay of organic solar cells based on three different ETLs: ZnO, c-In₂O₃, and a-In₂O₃. The photocurrent decay was measured under light illumination.

illumination is provided by using a white LED with the light intensity of 1 sun equiv. Among three devices, the c-In₂O₃ device exhibits the fastest photocurrent decay. The photocurrent decay time is derived by using an exponential decrease function. The photocurrent decay time in the c-In₂O₃ device is only 0.46 μ s lower than the ones observed in the other two counterparts, ZnO and a-In₂O₃, with the decay times of 0.61 and 0.88 μ s, respectively. The transient photocurrent is also measured without the background light illumination, as shown in Figure S9. It shows a similar trend, where the decay time for the c-In₂O₃ device is the lowest. From the transient photocurrent measurement, it can be concluded that the ETL with the higher mobility is better for charge extraction. The charge extraction in the c-In₂O₃ sample is more efficient than the one in the ZnO sample, which could be the main reason for the enhanced short circuit current.

Due to its high mobility and wide band gap, the sol-gel-processed In₂O₃ ETL is considered as a promising ETL candidate for solution-processed photovoltaic technologies.^{24,39} However, the occurrence of pinholes in the In₂O₃ layer during the annealing process is a critical issue in limiting the device performance.²⁴ Here, we successfully synthesized a

high quality solution-processed In₂O₃ ETL for organic photovoltaic via the incorporation of a small amount of additive, which significantly lowers the processing temperature. The solution-processed In₂O₃ ETLs are modified with a thin layer of PEIE, which effectively minimizes the pinholes and defects in the In₂O₃ layer and tunes the work function of In₂O₃ for a more efficient charge injection. Both fullerene-based and nonfullerene-based organic solar cells with the In₂O₃ ETL appear as a superior device compared to its counterpart, ZnO. The better device efficiency can be explained by the more efficient charge extraction and the more favorable blend morphology. Compared with ZnO film, c-In₂O₃ film shows the significantly higher mobility. Therefore, the faster charge collection is achieved in c-In₂O₃, resulting in the enhanced short circuit current. In order to fully understand the effects of mobility of ETLs on device performance, a series of In₂O₃ with different annealing temperatures are systematically studied. It is found that charge extraction shows a strong relationship with the mobility of the underlying ETL. As the annealing temperature decreases from 300 to 200 $^{\circ}$ C, In₂O₃ exhibits an amorphous microstructure. Although indium oxide shows a relatively excellent carrier mobility in the amorphous state compared with other semiconductors, such as silicon due to the different transport mechanisms, a lower processing temperature still leads to the increased trap states, which are confirmed by the XPS measurement.^{34,40,41} Compared with the crystalline indium oxide, significantly poorer charge extraction and higher recombination have been observed in the device with the amorphous indium oxide. Moreover, it is also interesting to note that the morphology of the active layer is sensitive to the microstructure of the underlying ETL. If the underlying layer exhibits some preferential orientations, it could act as a template to induce polymer crystallization into a certain orientation. Compared with ZnO and a-In₂O₃, the more highly aligned crystallites have been observed in the c-In₂O₃ layer. Therefore, the polymer deposited on the top of the c-In₂O₃ layer exhibits the more “face-on” configuration and better crystallite orientational ordering, leading to the faster charge transport.

The results presented in this study not only introduces a new ETL for organic photovoltaic with an excellent device performance but also provides general rules on how to design a highly efficient ETL. A high mobility ETL with a good surface coverage is necessary for the fast and efficient charge extraction. The modification of a thin layer of dipole molecules can further avoid the severe charge recombination in the pinhole area. In addition, as the polymer crystallization is strongly dependent on the microstructure of the underlying layer, the fabrication of the ETL with a controlled crystallite orientation is also of importance, which will assist the formation of a preferable polymer crystallization atop.

Conclusions. A solution-processed high mobility indium oxide ETL was synthesized for organic solar cells. After modification with a monolayer of PEIE, the average PCE of device based on this crystallized indium oxide shows a significant enhancement from 9.5% to 10.5% in PBDDTTT-EFT-PC₇₁BM solar cells and from 10.8% to 11.5% in PBDDTTT-EFT-IEICO-4F solar cells, compared with their counterparts based on zinc oxide. The high mobility of c-In₂O₃ enables a more efficient charge extraction at the interface between the active layer and ETL. Moreover, the aligned crystallite orientation of underlying In₂O₃ also induces the polymer crystallization into a favorable nanomorphology

facilitating the charge transport through the active layer. The emergence of the In_2O_3 ETL provides a new material platform for exploring the boundary of high performance OSCs.

■ ASSOCIATED CONTENT

Supporting Information

The Supporting Information is available free of charge on the ACS Publications website at DOI: 10.1021/acs.nanolett.8b02452.

Experimental methodology; XRD data; GIWAXS patterns; XPS; device performance of PBDTTT-EFT/IEICO-4F; 1D GIWAXS data plots (PDF)

■ AUTHOR INFORMATION

Corresponding Author

*E-mail: yangy@ucla.edu.

ORCID

Christopher McNeill: 0000-0001-5221-878X

Mingkui Wang: 0000-0002-4516-2500

Yang Yang: 0000-0001-8833-7641

Author Contributions

The manuscript was written through contributions of all authors. All authors have given approval to the final version of the manuscript.

Notes

The authors declare no competing financial interest.

■ ACKNOWLEDGMENTS

Y.Y. acknowledges the Air Force Office of Scientific Research (AFOSR) (FA2386-15-1-4108, FA9550e15-1e0610 and FA9550-15-1-0333), Office of Naval Research (ONR) (N00014-14-181-0648 and N00014-04-1-0434), National Science Foundation (NSF) (ECCS-1509955), and UC-Solar Program (MRPI 328368) for their financial support. Part of this research was performed in SAXS/WAXS beamline in Australian Synchrotron. All authors acknowledge Selbi Nuryyeva for help with English language editing.

■ REFERENCES

- Li, G.; Zhu, R.; Yang, Y. *Nat. Photonics* **2012**, *6*, 153–161.
- Xiao, S.; Zhang, Q.; You, W. *Adv. Mater.* **2017**, *29*, 1601391.
- Huang, W.; Cheng, P.; Yang, Y.; Li, G.; Yang, Y. *Adv. Mater.* **2018**, *30*, 1705706.
- An, Q.; Zhang, F.; Zhang, J.; Tang, W.; Deng, Z.; Hu, B. *Energy Environ. Sci.* **2016**, *9*, 281–322.
- Lu, L.; Zheng, T.; Wu, Q.; Schneider, A. M.; Zhao, D.; Yu, L. Recent Advances in Bulk Heterojunction Polymer Solar Cells. *Chem. Rev.* **2015**, *115*, 12666–12731.
- Yan, C.; Barlow, S.; Wang, Z.; Yan, H.; Jen, A. K. Y.; Marder, S. R.; Zhan, X. *Nat. Rev. Mater.* **2018**, *3*, 18003.
- Cheng, P.; Li, G.; Zhan, X.; Yang, Y. *Nat. Photonics* **2018**, *12*, 131–142.
- Che, X.; Li, Y.; Qu, Y.; Forrest, S. R. *Nat. Energy* **2018**, *3*, 422–427.
- Zhang, S.; Qin, Y.; Zhu, J.; Hou, J. *Adv. Mater.* **2018**, *30*, 1800868.
- Li, S.; Ye, L.; Zhao, W.; Yan, H.; Yang, B.; Liu, D.; Li, W.; Ade, H.; Hou, J. *J. Am. Chem. Soc.* **2018**, *140*, 7159.
- Fei, Z.; Eisner, F. D.; Jiao, X.; Azzouzi, M.; Röhr, J. A.; Han, Y.; Shahid, M.; Chesman, A. S. R.; Easton, C. D.; McNeill, C. R.; Anthopoulos, T. D.; Nelson, J.; Heeney, M. *Adv. Mater.* **2018**, *30*, 1705209.
- Sun, C.; Pan, F.; Bin, H.; Zhang, J.; Xue, L.; Qiu, B.; Wei, Z.; Zhang, Z.-G.; Li, Y. *Nat. Commun.* **2018**, *9*, 743.
- Lin, Y.; Zhao, F.; Prasad, S. K. K.; Chen, J. D.; Cai, W.; Zhang, Q.; Chen, K.; Wu, Y.; Ma, W.; Gao, F.; Tang, J. X.; Wang, C.; You, W.; Hodgkiss, J. M.; Zhan, X. *Adv. Mater.* **2018**, *30*, 1706363.
- Yu, G.; Gao, J.; Hummelen, J. C.; Heeger, A. J. *Science* **1995**, *270*, 1789–1791.
- Li, G.; Chu, C. W.; Shrotriya, V.; Huang, J.; Yang, Y. *Appl. Phys. Lett.* **2006**, *88*, 253503.
- Chen, L.-M.; Hong, Z.; Li, G.; Yang, Y. *Adv. Mater.* **2009**, *21*, 1434–1449.
- Huang, W.; Gann, E.; Cheng, Y.-B.; McNeill, C. R. *ACS Appl. Mater. Interfaces* **2015**, *7*, 14026–14034.
- Yang, G.; Tao, H.; Qin, P.; Ke, W.; Fang, G. *J. Mater. Chem. A* **2016**, *4*, 3970–3990.
- Sun, Y.; Seo, J. H.; Takacs, C. J.; Seifert, J.; Heeger, A. J. *Adv. Mater.* **2011**, *23*, 1679–1683.
- Liang, Z.; Zhang, Q.; Jiang, L.; Cao, G. *Energy Environ. Sci.* **2015**, *8*, 3442–3476.
- Liu, X.; Li, X.; Li, Y.; Song, C.; Zhu, L.; Zhang, W.; Wang, H.-Q.; Fang, J. *Adv. Mater.* **2016**, *28*, 7405–7412.
- Chen, H.-D.; Li, Y.-Q.; Zhu, J.; Zhange, Q.; Zhang, Q.; Xu, R.-P.; Li, C.; Zhang, Y.-X.; Huang, J.-S.; Zhan, X.; You, W.; Tang, J.-X. *Adv. Mater.* **2018**, *30*, 1706083.
- Park, S. H.; Roy, A.; Beaupré, S.; Cho, S.; Coates, N.; Moon, J. S.; Moses, D.; Leclerc, M.; Lee, K.; Heeger, A. J. *Nat. Photonics* **2009**, *3*, 297–303.
- Qin, M.; Ma, J.; Ke, W.; Qin, P.; Lei, H.; Tao, H.; Zheng, X.; Xiong, L.; Liu, Q.; Chen, Z.; Lu, J.; Yang, G.; Fang, G. *ACS Appl. Mater. Interfaces* **2016**, *8*, 8460–8466.
- Ke, W.; Fang, G.; Liu, Q.; Xiong, L.; Qin, P.; Tao, H.; Wang, J.; Lei, H.; Li, B.; Wan, J.; Yang, G.; Yan, Y. *J. Am. Chem. Soc.* **2015**, *137*, 6730–6733.
- Rim, Y. S.; Chen, H.; Liu, Y.; Bae, S.-H.; Kim, H. J.; Yang, Y. *ACS Nano* **2014**, *8*, 9680–9686.
- Kim, M.-G.; Kanatzidis, M. G.; Facchetti, A.; Marks, T. J. *Nat. Mater.* **2011**, *10*, 382.
- Rim, Y. S.; Chen, H.; Song, T.-B.; Bae, S.-H.; Yang, Y. *Chem. Mater.* **2015**, *27*, 5808–5812.
- Liao, S.-H.; Jhuo, H.-J.; Cheng, Y.-S.; Chen, S.-A. *Adv. Mater.* **2013**, *25*, 4766–4771.
- Chen, J.-D.; Cui, C.; Li, Y.-Q.; Zhou, L.; Ou, Q.-D.; Li, C.; Li, Y.; Tang, J.-X. *Adv. Mater.* **2015**, *27*, 1035–1041.
- Huang, W.; Gann, E.; Chandrasekaran, N.; Thomsen, L.; Prasad, S. K. K.; Hodgkiss, J. M.; Kabra, D.; Cheng, Y.-B.; McNeill, C. R. *Energy Environ. Sci.* **2017**, *10*, 1843–1853.
- Huang, W.; Gann, E.; Xu, Z.-Q.; Thomsen, L.; Cheng, Y.-B.; McNeill, C. R. *J. Mater. Chem. A* **2015**, *3*, 16313–16319.
- Zhou, Y.; Fuentes-Hernandez, C.; Shim, J.; Meyer, J.; Giordano, A. J.; Li, H.; Winget, P.; Papadopoulos, T.; Cheun, H.; Kim, J.; Fenoll, M.; Dindar, A.; Haske, W.; Najafabadi, E.; Khan, T. M.; Sojoudi, H.; Barlow, S.; Graham, S.; Brédas, J.-L.; Marder, S. R.; Kahn, A.; Kippelen, B. *Science* **2012**, *336*, 327–332.
- Yu, X.; Marks, T. J.; Facchetti, A. Metal oxides for optoelectronic applications. *Nat. Mater.* **2016**, *15*, 383–396.
- Huang, W.; Gann, E.; Thomsen, L.; Dong, C.; Cheng, Y.-B.; McNeill, C. R. *Adv. Energy Mater.* **2015**, *5*, 1401259.
- Verploegen, E.; Mondal, R.; Bettinger, C. J.; Sok, S.; Toney, M. F.; Bao, Z. *Adv. Funct. Mater.* **2010**, *20*, 3519–3529.
- Rivnay, J.; Mannsfeld, S. C. B.; Miller, C. E.; Salleo, A.; Toney, M. F. *Chem. Rev.* **2012**, *112*, 5488–5519.
- Huang, W.; Gann, E.; Chandrasekaran, N.; Prasad, S. K. K.; Chang, S.-Y.; Thomsen, L.; Kabra, D.; Hodgkiss, J. M.; Cheng, Y.-B.; Yang, Y.; McNeill, C. R. *Adv. Energy Mater.* **2017**, *7*, 1602197.
- Yoon, S.; Ha, T.-J.; Kang, D.-W. *Nanoscale* **2017**, *9*, 9754.
- Rim, Y. S.; Chen, H.; Kou, X.; Duan, H.-S.; Zhou, H.; Cai, M.; Kim, H. J.; Yang, Y. *Adv. Mater.* **2014**, *26*, 4273–4278.
- Nomura, K.; Ohta, H.; Takagi, A.; Kamiya, T.; Hirano, M.; Hosono, H. *Nature* **2004**, *432*, 488.